Electrical transport and dielectric relaxation in Fe_3O_4–polypyrrole hybrid nanocomposites

2005 J. Phys.: Condens. Matter 17 5895

(http://iopscience.iop.org/0953-8984/17/37/025)

INSTITUTE OF PHYSICS PUBLISHING JOURNAL OF PHYSICS: CONDENSED MATTER

J. Phys.: Condens. Matter **17** (2005) 5895–5910 doi:10.1088/0953-8984/17/37/025

Electrical transport and dielectric relaxation in Fe_3O_4–polypyrrole hybrid nanocomposites

Ashis Dey[1], **Amitabha De**[2] **and S K De**[1]

[1] Department of Materials Science, Indian Association for the Cultivation of Science, Jadavpur, Kolkata 700 032, India
[2] Chemical Sciences Division, Saha Institute of Nuclear Physics, 1/AF Bidhannagar, Kolkata 700 064, India

Received 16 March 2005, in final form 12 August 2005
Published 2 September 2005
Online at stacks.iop.org/JPhysCM/17/5895

Abstract

The polymerization of pyrrole in an aqueous medium in the presence of nanodimensional Fe_3O_4 using ammonium peroxodisulphate (APS) as oxidant results in the formation of polypyrrole–Fe_3O_4 nanocomposites. Characterization of the composites was carried out by Fourier transform infrared spectroscopy, x-ray diffraction, scanning and transmission electron microscopy. The magnetization data exhibit a small hysteresis loop at room temperature. The Mössbauer spectra at room temperature reveal the doublet structure, characteristic of the superparamagnetic phase in magnetite (Fe_3O_4). The composite samples reveal ordered semiconducting behaviour. Polypyrrole is the dominating component in the transport process of the nanocomposites. A very large dielectric constant of about 11 000 at room temperature has been observed. The interface between polypyrrole and Fe_3O_4 plays an important role in producing a large dielectric constant in the composite.

1. Introduction

Recently, conducting polymer nanocomposites with both electrical and ferromagnetic properties have generated tremendous attraction, and they have become one of the most active and promising research areas [1, 2]. These materials are largely being used in nonlinear optics, electrochemical display devices, molecular electronics, electrical and magnetic shields and microwave absorbing materials. The large surface to volume ratio of the nanoparticles results in the formation of composites with unusual physical and chemical properties. The properties of the composites are quite different from the constituent components due to interaction at the molecular level. The dielectric response of the composite systems is very complex; among different factors, the grain boundary plays a crucial role.

Magnetite (Fe_3O_4) has been extensively studied due to its variety of intriguing properties such as mixed valency, charge ordering and metal–insulator transition at low temperature [3]. At room temperature it is a poor metal, having conductivity [4] of about 2×10^2 S cm^{-1}.

It also exhibits half metallic behaviour [5] with high ferromagnetic transition temperature, 860 K. The metal–insulator transition occurs at about 120 K, and is known as the Verwey transition [6], with an increase of resistivity by two orders of magnitude accompanied by a structural change from cubic to monoclinic. The abrupt change in resistivity upon cooling is caused by ordering of Fe^{2+} and Fe^{3+} cations on the crystal sublattices [7, 8]. Thin films [9] and nanocrystals [10] of Fe_3O_4 exhibit anomalous behaviour in magnetic and transport properties compared to the bulk due to quantum size effects. Superparamagnetism [11], enhancement in magnetoresistance [12] and decrease of the Verwey transition temperature [10, 13] with reduction in size are observed. Composites of Fe_3O_4 with conducting polyaniline [14, 15], polypyrrole [16, 17] (PPY) and polyvinyl alcohol (PVA) [18] have been studied in the recent past. Most of the studies are concentrated on the magnetic and magnetotransport properties of magnetite. Here we have made an attempt to synthesize Fe_3O_4 nanoparticles inside a network of conducting polymer, and we have studied their transport and dielectric properties to investigate the underlying electronic conduction process.

2. Experimental details

Pyrrole (AR Grade) and ammonium peroxodisulphate (APS) were purchased from E. Merck, India. The monomer was vacuum distilled twice before use and was kept in the dark prior to use, while the APS was used as received.

Magnetic nanoparticles of Fe_3O_4 were synthesized by a standard co-precipitation technique. $FeCl_3{\cdot}6H_2O$ and $FeCl_2{\cdot}4H_2O$ taken in 2:1 molar ratio were separately dissolved in 10 ml of deionized water and stirred for 20 min at room temperature. The resulting mixture was then added dropwise under ultrasonic action to 400 ml of aqueous ammonia solution (0.6 M) in 30 min. The pH of the solution was kept at 11–12 with the addition of concentrated ammonium hydroxide solution. Finally the resulting nanoparticles were washed with deionized water several times to remove all the adhered impurities, and dried in a vacuum oven at 50 °C.

For the preparation of Fe_3O_4–polypyrrole nanocomposites, a dispersion of Fe_3O_4 nanoparticles was made by adding a known amount of Fe_3O_4 in 20 ml of deionized water under ultrasonic action. After 30 min pyrrole of known volume was slowly syringed into the dispersion under constant ultrasonic action at room temperature to get Fe_3O_4 nanoparticles impregnated with pyrrole. Then an aqueous solution of APS maintaining a pyrrole:APS mole ratio of 1:1.25 was added dropwise under sonication. A gradual change of colour from light black to deep black indicated the formation of polypyrrole (PPY). The solution was then kept under sonication for about an hour for complete polymerization followed by centrifugation at 10 000 rpm. The resulting nanocomposites came out as a black solid residue, which was washed thoroughly first with ethyl alcohol and then with deionized water several times to remove all the adhering impurities. Finally the composite samples were dried overnight in a vacuum oven at 50 °C. The compositions of the different nanocomposite samples studied are shown in table 1. The samples were pressed into pellets of diameter 8.5 mm by applying 5 ton pressure.

3. Characterization

The particle size of the bare Fe_3O_4 nanoparticles, the nanocomposites and the nature of interaction between the conducting and insulating components were determined using high-resolution transmission electron microscopic studies (HRTEM; JEM 2010). Infrared (IR) spectra of the bare Fe_3O_4 nanoparticles, polymer and the nanocomposites samples pelletized

Table 1. Weight percentage of pyrrole (x), room-temperature dielectric constant (ϵ_1) at 6.95 KHz, grain boundary (σ_{gb}) and grain (σ_g) conductivity, activation energy from grain conductivity (E_g) and activation energy (E_a) of dielectric relaxation.

Sample	x	ϵ_1	σ_{gb} (10^{-4} S cm^{-1})	σ_g (10^{-3} S cm^{-1})	E_g (meV)	E_a (meV)
CP1	90.6	10 665	2.76	6.23	69	70
CP2	85.3	5 281	2.38	5.13	73	77
CP3	80.6	3 115	0.32	0.63	79	90

with KBr were performed using a Fourier transform infrared (FTIR) spectrometer (Perkin-Elmer Model 1600). The x-ray diffraction (XRD) patterns of the nanocomposites were obtained using a Philips Diffractometer (PW 1710) with Cu Kα radiation. Magnetic measurements at room temperature were performed using vibrating sample magnetometer (Lakeshore 7400 VSM). The Mössbauer spectra were recorded in a standard PC based spectrometer working in the constant acceleration mode. A 10 mCi ^{57}Co in Rh matrix was used as the source. The system was calibrated with a high-purity α-Fe foil of thickness 12 μm.

The complex dielectric constants were obtained from the measurements of capacitance (C) and dissipation factor (D) by a 4192A Agilent impedance analyser up to the frequency of 1.6 MHz at different temperatures. The real part of relative dielectric constant ϵ_1 was evaluated by the relation $C = \epsilon_1\epsilon_0\, A/t$, where ϵ_0 is the vacuum permittivity, A is the area and t is the thickness of the sample. The imaginary component was calculated from the dissipation factor, $\epsilon_2 = D\epsilon_1$. The electrical contacts were made by silver paint.

4. Results and discussion

Figure 1 shows the characteristic peaks of the x-ray diffraction (XRD) pattern of the as-synthesized Fe_3O_4 nanoparticles and the nanocomposite sample (CP3) with highest Fe_3O_4 content. The main peaks at $2\theta = 30.2°$ (220), 35.54° (311), 43.2° (400), 53.5° (422) and 57.2° (511) which are characteristic of Fe_3O_4 are also present in the composite. A broad peak appears at 25.6° which is attributed to PPY, suggesting some degree of crystallinity in the PPY. During polymerization the growth of the polymer chain is restricted to some extent in the presence of Fe_3O_4 nanoparticles and the polymer becomes crystalline. The coherent length inside Fe_3O_4 nanoparticles of the composite is calculated following Scherrer's equation [19],

$$D = K\lambda/\beta\cos\theta \tag{1}$$

where $K = 0.89$, D represents the coherent length, λ the wavelength of Cu Kα radiation, and β the corrected value at half width (FWHM) of the diffraction peak. The peak at $2\theta = 35.5°$ (311), which is a characteristic peak of Fe_3O_4, was chosen to calculate D, and it comes out to be 10.2 nm.

Figures 2(a)–(c) show the FTIR spectra of the bare polypyrrole, nanocomposite samples CP3 and Fe_3O_4 nanoparticles respectively. The peaks at 1541 and 1456 cm^{-1} correspond to typical pyrrole ring vibrations [20, 21]. The peaks at 1300 and 1170 cm^{-1} are attributed to =CH in-plane vibration and the peaks at 784 and 898 cm^{-1} to =CH out-of-plane vibration. The band at 570 cm^{-1} appears in the composite samples, which is attributed to Fe_3O_4 [22]. Moreover, some of the peaks corresponding to PPY appear much sharper and stronger due to constrained growth of the polymer chain in the presence of Fe_3O_4. This indicates that there is some interaction between polypyrrole and the Fe_3O_4 nanoparticles.

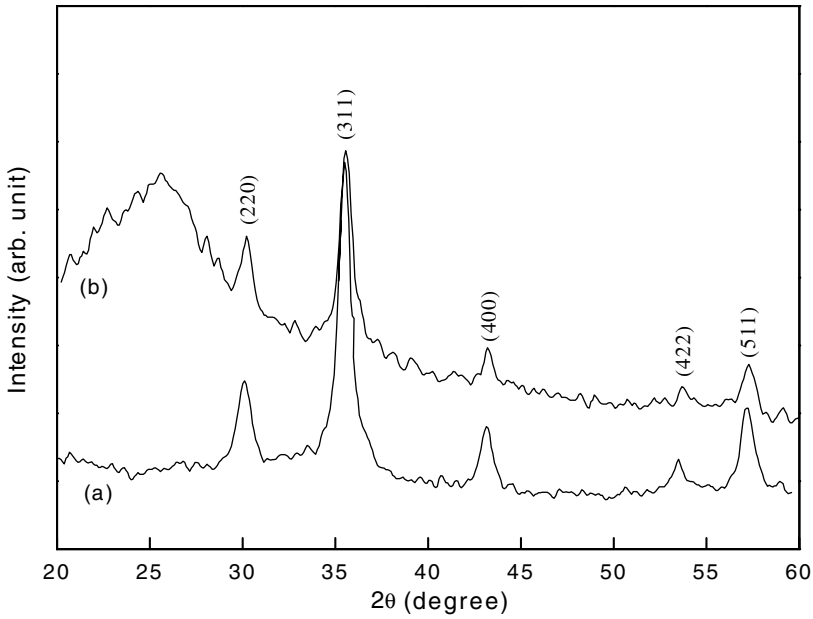

Figure 1. X-ray diffraction pattern of (a) bare Fe_3O_4 nanoparticles and (b) PPY–Fe_3O_4 nanocomposite (CP3).

Figures 3(a)–(c) show the scanning electron microscope (SEM) micrographs of three different nanocomposite samples. The grain size decreases with the increase of Fe_3O_4 loading in the composites. Moreover, the grains become more uniform with the increase of Fe_3O_4 content. High-resolution transmission electron microscope (HRTEM) micrographs of the as-synthesized nanocomposite sample CP3 are shown in figures 4(a) and (b). Figure 4(a) shows the lattice image from an Fe_3O_4 nanoparticle in the surroundings of the PPY matrix. The lattice spacing is found to be 0.147 nm, which corresponds to the (440) plane in Fe_3O_4. The fast Fourier transform (FFT) image (figure 4(a), inset) of CP3 has a diffused ring, indicating the presence of Fe_3O_4 in the network of the amorphous PPY matrix. Figure 4(b) shows a lower magnification image of the same composite, which indicates the nanoparticles to be well dispersed in the polymer matrix and to be of spherical shape with uniform diameter lying in the range from 20 to 30 nm. So it can easily be concluded that the Fe_3O_4 nanoparticles are not simply mixed up or blended with the polymer; rather, they are entrapped inside the polypyrrole chains. This fact is also supported by XRD and FTIR analyses.

The magnetization data of Fe_3O_4 nanoparticles and the composite CP3 at room temperature are presented in figures 5(a) and (b). The curves as shown in enlarged form near the origin in the inset of figure 5 demonstrate a small hysteresis loop. Remanent magnetization of 0.49 emu g^{-1} and a coercive field (H_c) of about 19 G are observed for Fe_3O_4. The saturation magnetization (M_s) is 42 emu g^{-1}. The magnetic properties are significantly lower than those of the bulk, $M_s \approx 84$ emu g^{-1}, $H_c \approx 500$–800 G [23]. The reduction of M_s may be due to the quantum size effect, surface spin disorder and antiphase boundaries [24]. Both the saturation and remanent magnetizations decrease to 5.1 and 0.11 emu g^{-1} respectively for CP3. The significant decrease of M_s in the nanocomposite is due to the reduction of Fe_3O_4 content. A larger coercive field of 31 G is found in the nanocomposite. Thus the nanoparticles and the nanocomposites exhibit weak ferromagnetic behaviour with very low coercive field.

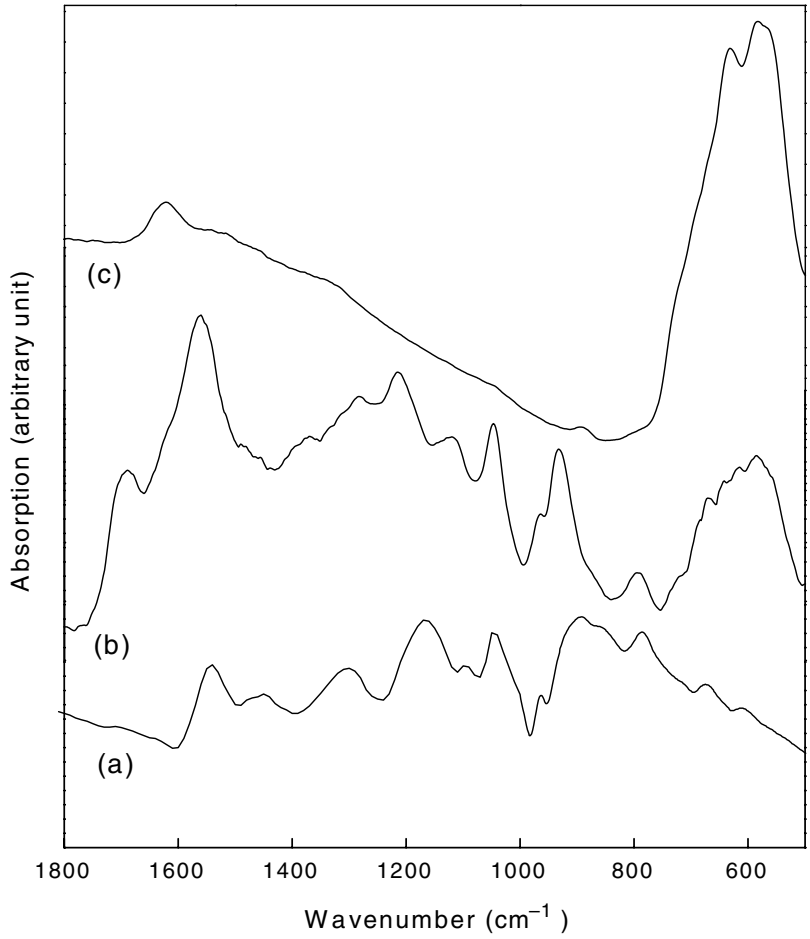

Figure 2. Fourier transform infrared (FTIR) spectra of (a) pure PPY (b) nanocomposite sample (CP3) and (c) bare Fe_3O_4 nanoparticles respectively.

Figures 6(a) and (b) show the Mössbauer spectra of the bare magnetite (Fe_3O_4) and the sample CP3 recorded at room temperature. The spectrum was de-convoluted into a distribution of sextets along with a crystalline doublet. Fitting of the magnetically split part with a distribution was necessary because of the broad Mössbauer absorption lines. This may be due to the particle size distribution present in the sample. The hyperfine parameters of the sextet obtained from the 'NORMOS' fitting programme [25] gave an isomer shift (IS) 0.36 mm s^{-1}, negligible quadrupole splitting (QS) (<0.01) and an average hyperfine field (H_{int}) 47 T. These parameters agree well with those of magnetite. The fitted parameters IS and QS of the doublet are 0.59 and 0.71 mm s^{-1} respectively. The high QS suggests that the particles are experiencing a higher electric field gradient (EFG). This is a common phenomenon with ultrafine magnetic particles. The presence of this doublet is attributed to ultra-fine magnetite particles undergoing superparamagnetic (SPM) relaxation. The fraction of atoms undergoing SPM relaxation as estimated from the area of the doublet is about 41%. The spectrum of CP3 as shown in figure 6(b) was also fitted with a distribution of hyperfine fields along with a broad crystalline singlet. The parameters obtained from the deconvolution of the sextet give

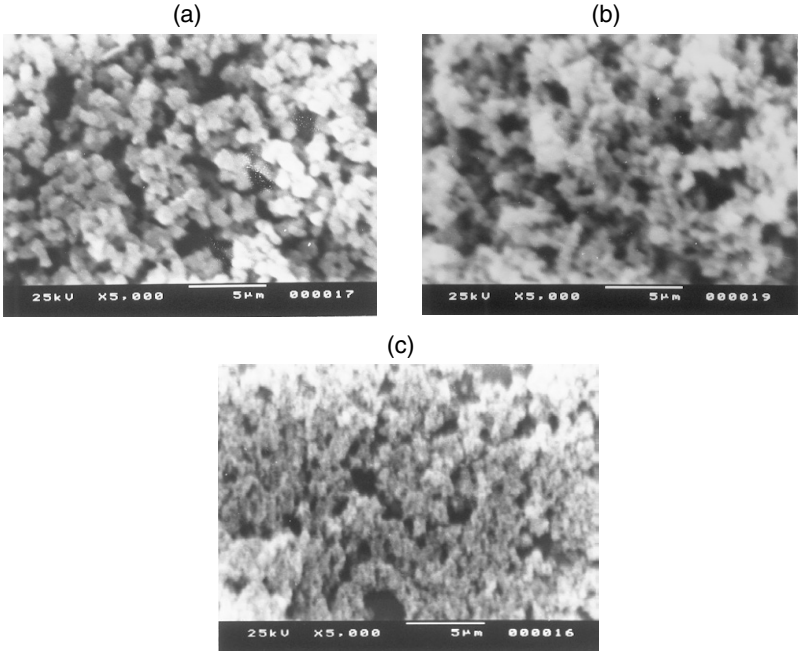

Figure 3. SEM micrograph of the cold-pressed powder samples (a) CP1, (b) CP2 and (c) CP3, respectively.

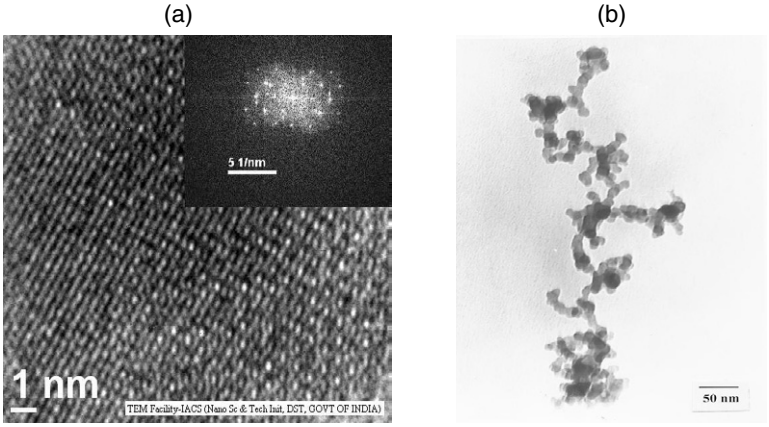

Figure 4. TEM micrograph of sample CP3. (a) High-resolution lattice image; the inset is the FFT image of the same sample. (b) Lower magnification image of CP3.

an IS $= 0.49$ mm s^{-1}, QS $= 0.01$ mm s^{-1}, and $H_{\text{int}} = 47$ T. The increase in the isomer shift of this sample with respect to the bare magnetite may be due to electron exchange with the oxygen present in the polypyrrole. The isomer shift of the singlet is 0.4 mm s^{-1}. The relative fraction of SPM atoms is about 30%. The singlet with broad FWHM in this case indicates that the EFG is not large enough to split it into a doublet as observed in the case of bare magnetite. The lower EFG in the case of the sample CP3 compared with the bare sample indicates that its average particle size is more than that of the bare sample.

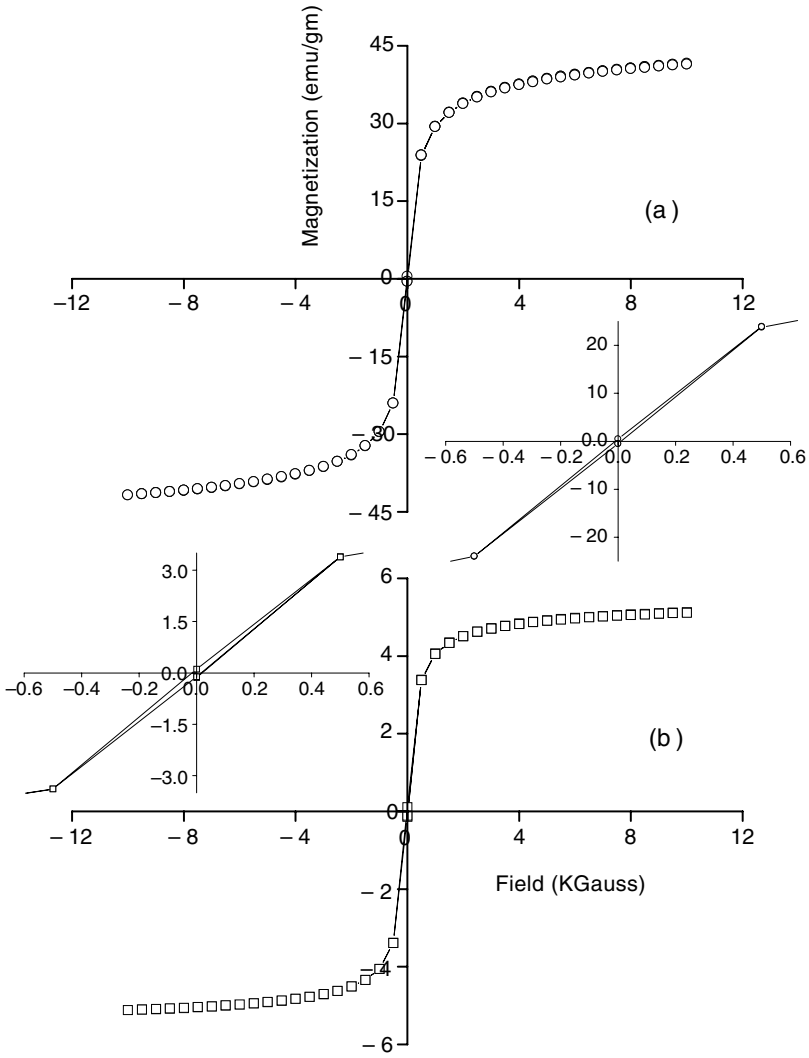

Figure 5. Room-temperature magnetization curve of (a) as-synthesized Fe_3O_4 nanoparticles and (b) the nanocomposite sample CP3.

The complex impedance ($Z = Z' + iZ''$) spectra at different temperatures for three different samples have been studied. The plots of Z' versus Z'' of the sample (CP3) with highest content of Fe_3O_4 are shown in figure 7. A single semicircular arc was found at room temperature. Lowering of temperature induced two semicircles. The number and shape of the semicircles depend on temperature. The appearance of two semicircles at low temperature suggests a contribution arising from both the grain and grain boundary regions of the polycrystalline samples. An equivalent circuit consisting of two parallel combinations of resistance (R) and capacitance (C) is usually used to interpret the complex impedance data as exhibited in figure 7. Ideally each RC element of the circuit gives rise to a semicircle. The position of the arc depends on the time constant RC of the individual circuit. The values of R and C for a grain boundary are larger compared to those for a grain. As a result of this

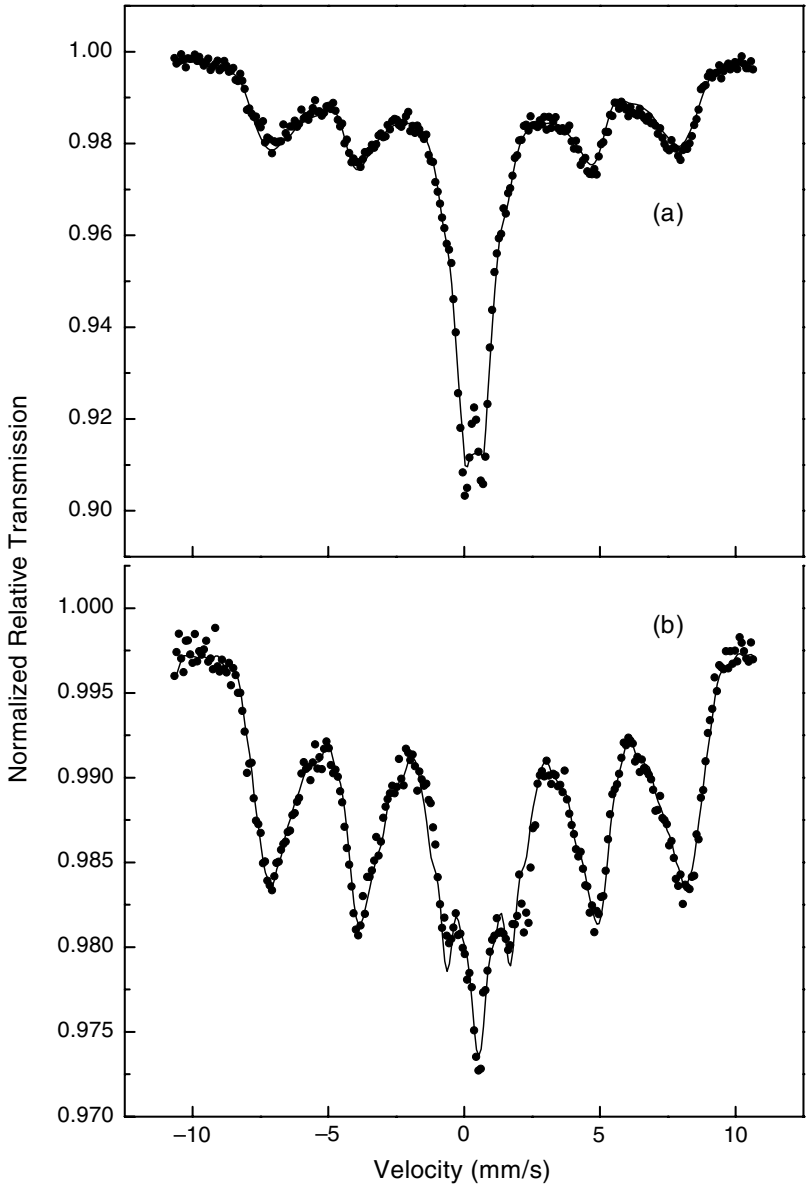

Figure 6. Mössbauer spectra of (a) bare Fe_3O_4 nanoparticles and (b) the nanocomposite sample CP3 at room temperature.

the arc maximum frequencies $\omega_{\max} = \frac{1}{RC}$ of the impedance plot are in the lower frequency region corresponding to a grain boundary effect. The observation of a single arc indicates that the circuit components of a grain boundary are much higher than those of a grain. The grain boundary effect dominates at room temperature. The grain boundary resistance increases with lowering of the temperature, and consequently the maximum of the arc in the impedance plot shifts towards lower frequency and lies outside the available frequency range. The increase of grain resistance upon decreasing the temperature induces a second semicircle in the higher frequency region.

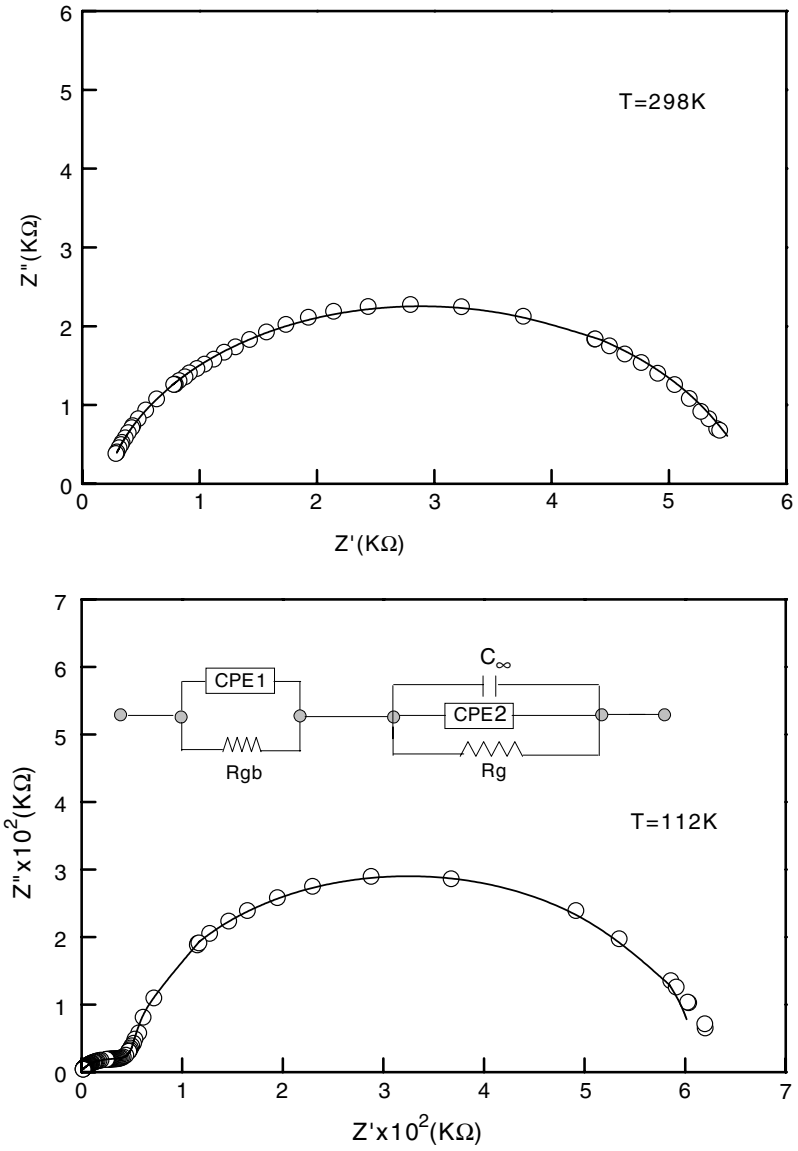

Figure 7. Impedance spectra of the sample CP3 at two representative temperatures. The solid lines are fits to the proposed equivalent circuit for the sample.

The impedance data were simulated by the equivalent circuit as shown in figure 7. This circuit consists of two parallel combinations of resistance and capacitance corresponding to two semicircles in impedance plot. In the modelled circuit R_g and R_{gb} represent the frequency-independent resistances of a grain and a grain boundary, respectively. The constant phase element (CPE) capacitors $C(\omega) = A(i\omega)^{n-1}$ are assumed to describe the more flattened semicircles [26, 27]. The parameter A is a constant for a given set of experimental data. The exponent n varies between 0 and 1. The CPE behaves as an ideal capacitor for $n = 1$ and an ideal resistor for $n = 0$. The experimental data are best fitted employing the complex nonlinear

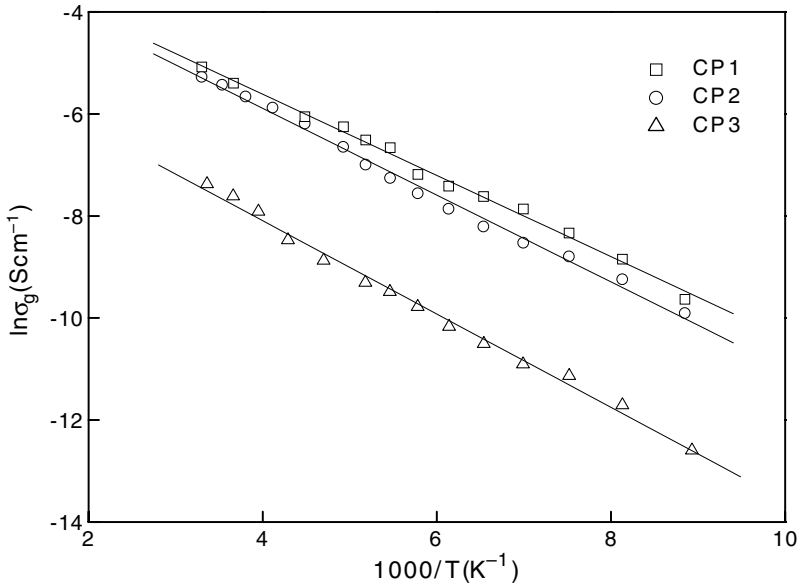

Figure 8. Arrhenius plot of grain conductivity for the three different samples CP1, CP2 and CP3, respectively.

curve-fitting LEVM program developed by Macdonald [28]. The solid lines in figure 7 represent the best fitted calculated values. The parallel RC combination at low frequency is (R_{gb}, C_{gb}), and it is(R_g, C_g) at high frequency, corresponding to grain boundary and grain respectively. The capacitor C_∞ is introduced in the circuit to take into account of the non-zero value of capacitance at high frequency. Grain (σ_g) and grain boundary (σ_{gb}) conductivities are evaluated from the best fitted values of R_g and R_{gb}. Both the conductivities decrease on raising the concentration of Fe_3O_4, as shown in table 1. The temperature dependences of σ_g for the three samples are shown in figure 8. In all the samples, the grain boundary conductivity is about one order of magnitude less than that of a grain, as depicted in table 1. Arrhenius-type behaviour for σ_g is found. The activation energy increases from 69 to 79 meV with increase of Fe_3O_4 content, as shown in table 1. Both C_{gb} and C_g are almost independent of temperature, unlike R_{gb} and R_g.

Each grain consists of PPY and Fe_3O_4 particle and the conductivity of the grain is far below that from the individual components. The conductivity of pure PPY is 9.44×10^{-2} S cm^{-1}, which is about four orders of magnitude less than that of bulk Fe_3O_4 (2×10^2 S cm^{-1}). Thus the conductivity of the nanocomposite should increase with increasing content of Fe_3O_4, but this contradicts the experimental results. The specific amount (weight) of PPY is higher than that of the oxide particles. The conductivity of the polymers primarily depends on the conjugation length. In the synthesis process, monomer pyrrole is first adsorbed on the surface of a Fe_3O_4 particle. Upon the addition of oxidant, polymerization takes place on the surface of each particle. The effective surface area increases with the increase of Fe_3O_4 concentration, and as result, the amount of pyrrole associated with each Fe_3O_4 particle is diminished. The chain length and consequently the conductivity are reduced with increase of particle content. The conductivity arises from the polymer component of the nanocomposite.

The temperature variation of the conductivity of PPY is well described by Mott's variable range hopping formalism [29]. This is applicable only in amorphous semiconductors. The

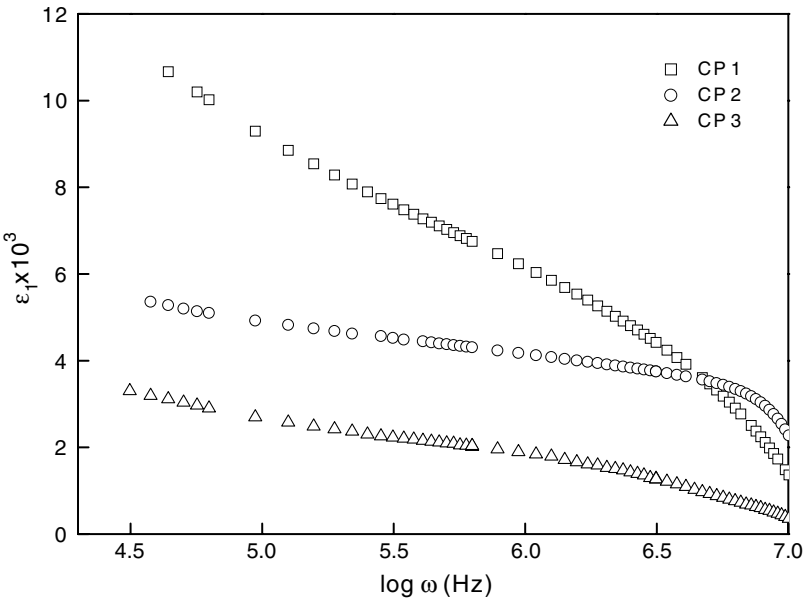

Figure 9. Frequency dependence of the real part of the relative dielectric permittivity (ϵ_1) at room temperature for samples CP1, CP2 and CP3 respectively.

linear relationship in the $\ln \sigma_g$ versus $1/T$ plot as shown in figure 8 indicates that the PPY in the composite is more ordered than pure PPY prepared in the absence of oxide particles. Larger activation energy implies higher potential barrier in the conduction process originating from the reduction of the polymer chain length. This is also consistent with the variation of Fe_3O_4 content. The room-temperature conductivity of cold-pressed powder Fe_3O_4 nanocrystals is very low compared with the intrinsic conductivity of the compound. The thermal activation energy as obtained from the conductivity of magnetite nanoparticles [30] is about 280 meV, much larger than 60–80 meV of the nanocomposite. The lower conductivity and higher activation energy are due to the poor contact between powder particles. Dispersion of nanosized magnetite in the matrix of conducting polymer introduces more conducting paths, resulting in higher conductivity. Magnetite exhibits anomalous behaviour in conductivity at low temperature, 120 K. No such changes in conductivity were found down to 112 K. The magnitude of the conductivity and its temperature variation suggest that the electrical properties of the nanocomposite are quite different from those of PPY and Fe_3O_4.

The variations of relative dielectric constant with frequency at room temperature for different compositions are presented in figure 9. A very high ϵ_1 of around 11 000 is found in sample CP1, but this decreases significantly with frequency as shown in figure 9. This value decreases with increase of Fe_3O_4 and is almost independent of frequency. The temperature variation of ϵ_1 for sample CP1 is shown in figure 10. Higher temperature leads to larger dielectric constant. The temperature dependence of ϵ_1 of single crystal Fe_3O_4 exhibits maxima at about 30–40 K. The highest value of the dielectric constant [31, 32] in Fe_3O_4 is about 400. This decreases continuously with increase of temperature. At room temperature it is below 100. The value of ϵ_1 for PPY is approximately 1000. The present observation of ϵ_1 is remarkable as it is larger than that of the constituent materials by ten times.

The relative dielectric loss spectra ϵ_2 as a function of frequency are shown in figure 11 at selected temperatures for sample CP1. The spectra exhibit broad peaks at low temperatures.

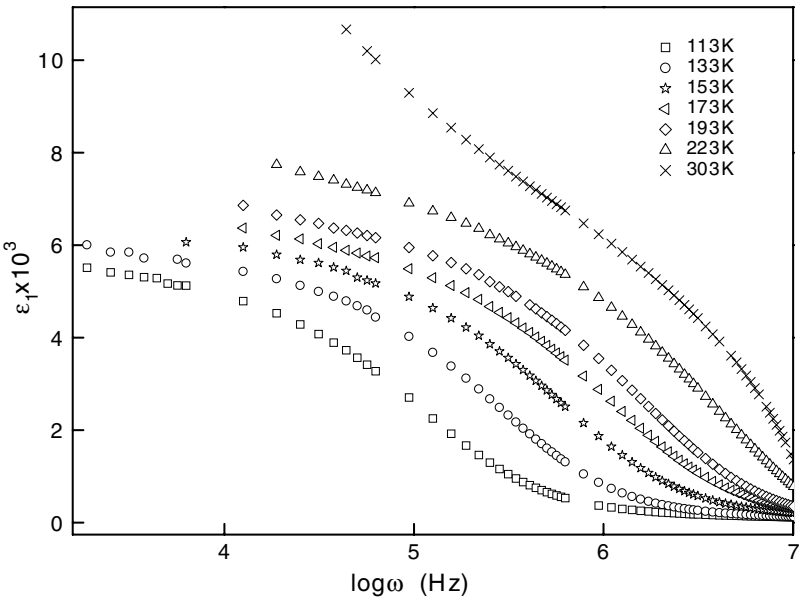

Figure 10. Frequency dependence of the real part of the relative dielectric permittivity (ϵ_1) at different temperatures for sample CP1.

The peak frequency shifts to higher frequency with increase of temperature. The complete loss spectra at higher temperature are not observed due to our experimental limitations. A quantitative analysis of the complex dielectric permittivity was performed by using the Cole–Cole relation [27].

$$\epsilon^* = \epsilon_\infty + \frac{\epsilon_s - \epsilon_\infty}{1 + (i\omega\tau)^\alpha} \tag{2}$$

where τ is the average relaxation time which is given at the frequency of maximum dielectric loss. The difference $\Delta\epsilon = \epsilon_s - \epsilon_\infty$ is known as the dielectric relaxation strength. The parameter α describes the distribution of the relaxation time of the system. The Cole–Cole expression reduces to classical Debye form for $\alpha = 1$. Excellent fits for the dielectric function were obtained for all temperatures. Hence, the Cole–Cole function is adequate to describe the dielectric relaxation in the nanocomposites. The best fitted parameters are shown in table 2. The dielectric strength ($\Delta\epsilon$) increases with increase of temperature.

The values of α as shown in table 2 are different from unity, which implies a non-Debye relaxation process at low temperature. The distribution function [26] of the relaxation time τ represented by equation (2) is given by

$$F(t/\tau) = \frac{1}{2\pi} \frac{\sin \alpha\pi}{\cosh[(1-\alpha)\ln(t/\tau)] - \cos\alpha\pi}. \tag{3}$$

The distribution of relaxation times for CP1 at three particular temperatures are shown in figure 12. The deviation of α from unity indicates the broad distribution of relaxation time in the spectrum. The distribution broadens with increase of temperature.

The relaxation time, τ, at different temperatures was determined from the reciprocal of the peak frequency. The Arrhenius plots of $\ln\tau$ against $1/T$ for the three different samples are shown in figure 13. A straight line behaviour is obtained. Thus the temperature dependence of the relaxation time of loss can be described by $\tau \propto \exp(E/kT)$, where E is the activation

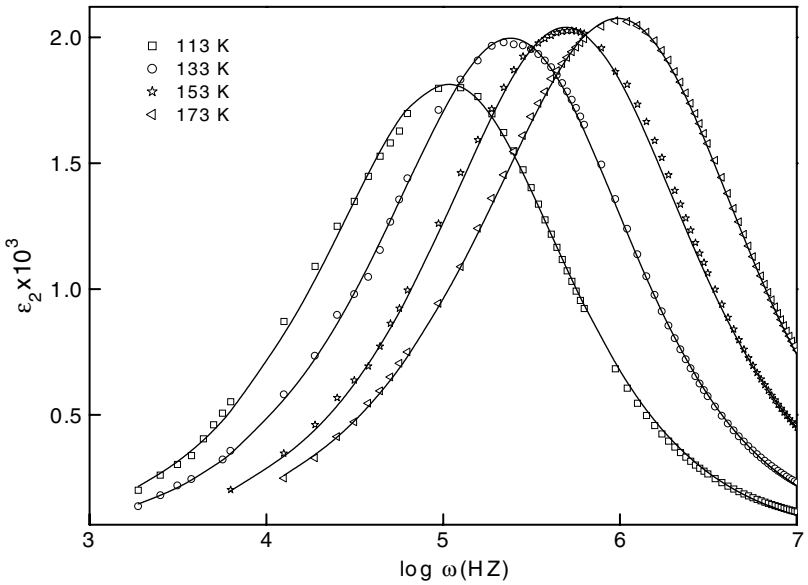

Figure 11. Frequency dependence of the imaginary part of the relative dielectric permittivity (ϵ_2) at selected temperatures for sample CP1. The solid lines are fits to equation (2).

Table 2. Dielectric strength ($\Delta\varepsilon$) and Cole–Cole (CC) function best fitted parameters τ and α in equation (2) for dielectric loss spectra of sample CP1.

Temperature (K)	($\Delta\varepsilon$)	τ (10^{-6} s)	α
113	5071	8.07	0.777
123	5208	4.46	0.770
133	5655	3.20	0.758
143	5672	2.11	0.753
153	5808	1.74	0.745
163	5894	1.09	0.740
173	6083	0.67	0.725
183	6249	0.48	0.714
193	6321	0.43	0.710
203	6357	0.30	0.699

energy of the dielectric process and k is the Boltzmann constant. The slope of the best fitted straight line gives the activation energy as given in table 1 for the three samples. The estimated values of activation energy are very close to that of the grain conductivity.

In heterogeneous systems, free carriers are immobilized. Maxwell–Wagner type polarization [33] can occur in such materials. Upon the application of alternating voltage, the mobile charges are blocked at the interface of different conductivity and permittivity and they provide the large value of dielectric permittivity. A high degree of dispersion in ϵ_1 is found at low frequencies for sample CP1. The grain boundary contribution dominates in this region. For the other two compositions, ϵ_1 remains almost independent of frequency, which implies that the grain is the source of the high dielectric response. In the Maxwell–Wagner two-layer model [34], the dielectric function depends on the conductivity and permittivity of the two layers. The static dielectric permittivity ϵ_s and the relaxation time τ based on the

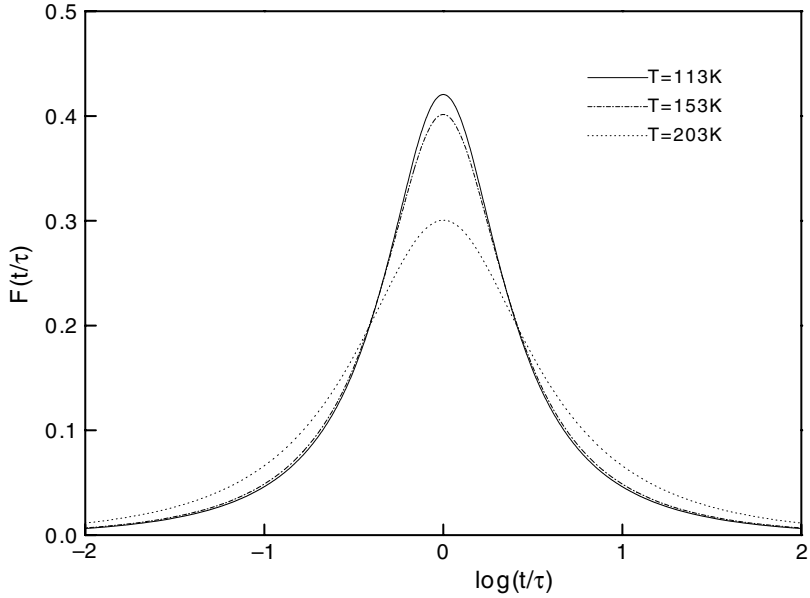

Figure 12. Distribution function (equation (3)) of the relaxation time of sample CP1 at three representative temperatures.

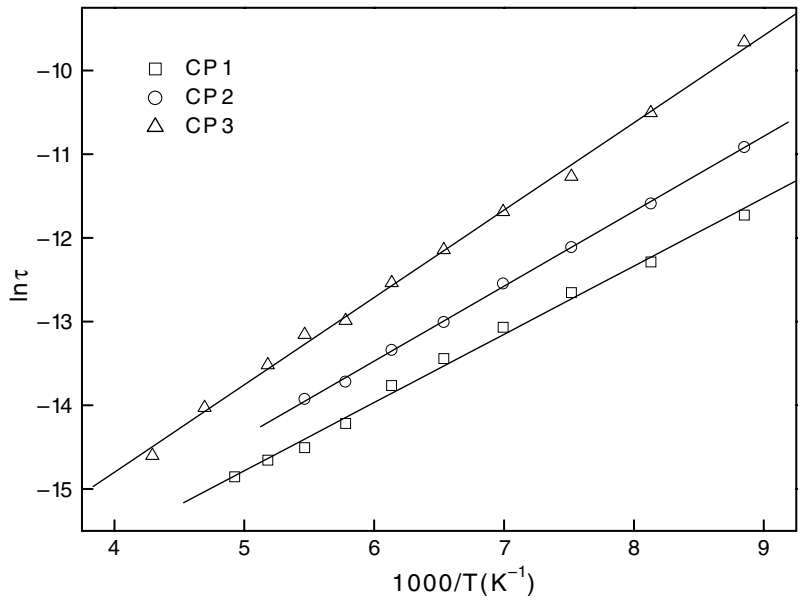

Figure 13. Temperature dependence of the dielectric relaxation time for the different samples.

two-layer model can be expressed as [34]

$$\epsilon_s = \frac{R_g \tau_g + R_{gb} \tau_{gb}}{C_0 (R_g + R_{gb})^2} \tag{4}$$

$$\tau = \frac{R_g \tau_{gb} + R_{gb} \tau_g}{R_g + R_{gb}} \tag{5}$$

where $\tau_g = R_g C_g$, $\tau_{gb} = R_{gb} C_{gb}$ and C_0 is the geometrical capacitance of the sample. Experimentally, $R_{gb} \gg R_g$ and $C_{gb} \gg C_g$ and the approximate ϵ_s and τ are given by

$$\epsilon_s = C_{gb}/C_0 \tag{6}$$

$$\tau = R_g C_{gb}. \tag{7}$$

Equation (6) demonstrates that the dielectric constant mainly depends on the grain boundary capacitance. The grain conductivity decreases with increase of Fe_3O_4 concentration, as shown in table 1. The charge carrier concentration decreases, which results in a decrease of grain boundary capacitance. The grain size also decreases with increasing Fe_3O_4 content. Hence the reduction in grain boundary capacitance and grain size give rise to a decrease in dielectric constant. The increase of dielectric permittivity with temperature is due to the enhanced value of conductivity at higher temperature.

The peak frequency $\omega_p = 1/\tau$ of ϵ_2 can be determined from the grain resistance, equation (7). The semiconducting behaviour of the grains suggests that an increase of temperature gives rise to a shift of the peak to higher frequencies, similar to experimental observations. This also indicates that the activation energy of the dielectric process is equivalent to the grain conduction process due to the weak temperature dependence of the grain boundary capacitance. From table 1 it is evident that the activation energies of these two processes are very close to each other. The Maxwell–Wagner-type relaxation in an inhomogeneous system follows the Debye formalism with a single relaxation time. The large dielectric constant and broad distribution of relaxation time in the nanocomposite are interpreted by a Maxwell–Wagner-type polarization and Cole–Cole dielectric function respectively. The distribution of grain size and conductivity or the inhomogeneous behaviour of the conductivity of the grains may give rise to a distribution of relaxation time, and consequently broadens the dielectric relaxation peak.

5. Conclusion

Magnetic properties such as the saturation magnetization and coercive field of the nanocomposite deviate significantly from bulk Fe_3O_4 values. The lower value of electric field gradient derived from Mössbauer spectra suggests that the average particle size of Fe_3O_4 in the nanocomposites is higher than that of bare Fe_3O_4 nanoparticles. The grain and grain boundary contributions to the conductivity in Fe_3O_4–polypyrrole nanocomposite were analysed by impedance spectroscopy. The grain size, and the grain and grain boundary conductivities decrease with increase of Fe_3O_4 concentration. The nanocomposites exhibit very high dielectric constant at low frequency. The magnitude and the frequency dependence of the dielectric permittivity are dependent on the content of Fe_3O_4 nanoparticles. A Maxwell–Wagner-type interfacial polarization leads to a high dielectric constant in the nanocomposite. The large dielectric constant of the nanocomposite indicates possible applications in the field of actuators and sensors.

Acknowledgments

This work is funded by the Department of Atomic Energy, Government of India (Project sanction No 2001/37/4/BRNS). Ashis Dey is thankful to the Council of Scientific and Industrial Research, Government of India for providing fellowship. The authors are grateful to the

Materials Science Division, UGC-DAE Consortium for Scientific Research, Kolkata for Mössbauer measurements.

References

[1] Gangopadhyay R and De A 2000 *Chem. Mater.* **12** 608
[2] Nalwa H S (ed) 2003 *Handbook of Organic–Inorganic Hybrid Materials and Nanocomposites* (California: American Scientific Publishers) R Gangopadhyay and A De, chapter (H-Conducting Polymer Nanocomposites)
[3] Garcia J and Subias G 2004 *J. Phys.: Condens. Matter* **16** R145
[4] Coey J M D, Berkowitz A E, Balcells L, Putris F F and Parker F T 1998 *Appl. Phys. Lett.* **72** 734
[5] Jeng H-T and Guo G Y 2002 *Phys. Rev.* B **65** 094429
[6] Verwey E J W 1939 *Nature* **144** 327
[7] Verwey E J W *et al* 1947 *J. Chem. Phys.* **14** 181
[8] Leonov I, Yaresko A N, Antonov V N, Korotin M A and Anisimov V I 2004 *Phys. Rev. Lett.* **93** 146404
[9] Lu Y X, Claydon J S, Xu Y B, Thompson S M, Wilson K and van der Laan G 2004 *Phys. Rev.* B **70** 233304
[10] Poddar P, Fried T and Markovich G 2002 *Phys. Rev.* B **65** 172405
[11] Voogt F C, Palstra T T M, Niesen L, Rogojanu O C, James M A and Hibma T 1998 *Phys. Rev.* B **57** R8107
[12] Venkatesan M, Nawka S, Pillai S C and Coey J M D 2003 *J. Appl. Phys.* **93** 8023
[13] Yang J B, Zhou X D, Yelon W B, James W J, Cai Q, Gopalakrishnan K V, Malik S K, Sun X C and Nikles D E 2004 *J. Appl. Phys.* **95** 7540
[14] Deng J, Ding X, Zhang W, Peng Y, Wang J, Long X, Li P and Chan A S C 2002 *Polymer* **43** 2179
[15] Zhang Z and Wan M 2003 *Synth. Met.* **132** 205
[16] Chen W, Li X, Xue G, Wang Z and Zou W 2003 *Appl. Surf. Sci.* **218** 216
[17] Chen A, Wang H, Zhao B and Li X 2003 *Synth. Met.* **139** 411
[18] Novakova A A, Lanchinskaya V Y, Volkov A V, Gendler T S, Kiseleva T Y, Moskvina M A and Zezin S B 2003 *J. Magn. Magn. Mater.* **258/259** 354
[19] Klug H P and Alexander L E 1954 *X-ray Diffraction Procedures for Polycrystalline and Amorphous Materials* (New York: Wiley) p 491
[20] Kostic R, Rakovic D, Stepanyan S A, Davidiva I E and Gribov L A 1995 *J. Chem. Phys.* **102** 3104
[21] Street B 1986 *Handbook of Conducting Polymers* vol 1 (New York: Dekker) p 256
[22] Nyquist R and Kagel R 1971 *Infrared Spectra of Inorganic Compounds* (New York: Academic)
[23] Craik D J 1981 *Magnetic Oxides,* Part 2 (New York: Wiley)
[24] Margulies D T, Parker F T, Redee M L, Spada F E, Chapman J N, Aitchison P R and Berkowitz A E 1997 *Phys. Rev. Lett.* **79** 5162
[25] Brand R A 1987 *Nucl. Instrum. Methods* B **28** 398
[26] Macdonald J R 1987 *Impedance Spectroscopy* (New York: Wiley)
[27] Jonscher A K 1983 *Dielectric Relaxation in Solids* (UK: Chesla Dielectric Group)
[28] http://www.solartonanalytical.com/downloads/downloads.html
[29] Ghosh M, Barman A, Das A, Meikap A K, De S K and Chatterjee S 1998 *J. Appl. Phys.* **83** 4230
[30] Liu K, Zhao L, Klavins P, Osterloh F E and Hiramatsu H 2003 *J. Appl. Phys.* **93** 7951
[31] Akishige Y, Fukatsu T, Kobayashi M and Sawaguchi E 1985 *J. Phys. Soc. Japan* **54** 2323
[32] Kobayashi M, Akishige Y and Sawaguchi E 1986 *J. Phys. Soc. Japan* **55** 4044
[33] Maxwell J C 1998 *A Treatise on Electricity and Magnetism* vol 1 (Oxford: Oxford University Press)
[34] Hippel V 1954 *Dielectrics and Waves* (New York: Wiley)